Repository Istituzionale dei Prodotti della Ricerca del Politecnico di Bari

Computing supersonic non-premixed turbulent combustion by an SMLD flamelet progress variable model

This is a post print of the following article

Original Citation:
Computing supersonic non-premixed turbulent combustion by an SMLD flamelet progress variable model / Coclite, Alessandro; Cutrone, Luigi; Gurtner, M.; DE PALMA, Pietro; Haidn, O. J.; Pascazio, Giuseppe. - In: INTERNATIONAL JOURNAL OF HYDROGEN ENERGY. - ISSN 0360-3199. - 41:1(2016), pp. 632-646. [10.1016/j.ijhydene.2015.10.086]

Availability:
This version is available at http://hdl.handle.net/11589/62257 since: 2021-03-15

Published version
DOI:10.1016/j.ijhydene.2015.10.086

Terms of use:

(Article begins on next page)

09 April 2024

*Manuscript
Click here to view linked References

Computing supersonic non-premixed turbulent combustion by an SMLD flamelet progress variable model

A. Coclite[a,b], L. Cutrone[c,b], M. Gurtner[d], P. De Palma[a,b], O. J. Haidn[d], G. Pascazio[a,b,*]

[a] *Dipartimento di Meccanica, Matematica e Management (DMMM), Politecnico di Bari, Via Re David 200 – 70125 Bari, Italy*
[b] *Centro di Eccellenza in Meccanica Computazionale (CEMeC), Politecnico di Bari, Via Re David 200 – 70125 Bari, Italy*
[c] *Centro Italiano Ricerche Aerospaziali (CIRA), via Maiorise – 81043 Capua, Italy*
[d] *Institute for Flight Propulsion (LFA), Technische Universität München, Boltzmannstrasse 15 – 85748, Garching, Germany*

Abstract

This paper presents a statistical more likely distribution (SMLD) approach for the evaluation of the presumed probability density function (PDF) in flamelet progress variable (FPV) models for non-premixed supersonic combustion. The numerical simulation of the NASA Langley Research Center supersonic H_2-Air combustion chamber is performed using two approaches: the first one is a standard FPV model, built presuming the functional shape of the PDFs of the mixture fraction, Z, and of the progress parameter, Λ; the second approach employs the SMLD technique to presume the joint PDF of Z and Λ. The standard and FPV-SMLD models have been developed using the low Mach number assumption. In both cases, the temperature is evaluated by solving the total-energy conservation equation, providing a more suitable approach for the simulation of supersonic combustion. By comparison with experimental data, the proposed SMLD model is shown to provide a clear improvement with respect to the standard FPV model, especially in the auto-ignition and stabilization regions of the flame.

Keywords: Joint Presumed PDF modelling, Hydrogen-Air combustion, Reynolds-Averaged Navier–Stokes equations

Nomenclature

C	= Progress variable $[-]$
D_ϕ	= Diffusivity of ϕ $[m^2/s]$
H	= Specific total enthalpy $[J/kg]$
k	= Turbulent kinetic energy $[m^2/s^2]$
Ma	= Mach number $[-]$
p	= Pressure $[Pa]$
$\widetilde{P}(x)$	= Density-weighted probability density function
q	= Heat flux $[J/(m^2\,s)]$
$\dot{q}_{react}$	= Heat release rate $[J/(m^2\,s)]$
Re	= Reynolds number $[-]$
T	= Temperature $[K]$
Tu	= Turbulence intensity $[-]$
u	= Velocity $[m/s]$
Y_ϕ	= Mass fraction of species ϕ $[-]$

*Corresponding author
Email addresses: alessandro.coclite@poliba.it (A. Coclite), l.cutrone@cira.it (L. Cutrone), gurtner@lfa.mw.tum.de (M. Gurtner), pietro.depalma@poliba.it (P. De Palma), haidn@lfa.mw.tum.de (O. J. Haidn), giuseppe.pascazio@poliba.it (G. Pascazio)

The publisher version is acknowledged at
http://dx.doi.org/10.1016/j.ijhydene.2015.10.086

Z = Mixture fraction $[-]$
$\beta(x)$ = β-distribution
$\Gamma(x)$ = Euler function
$\delta(x)$ = Dirac distribution
Λ = Progress parameter $[-]$
μ = Dynamic viscosity $[Pa\,s]$
μ_x = Lagrangian multiplier
ν = Kinematic viscosity $[m^2/s]$
ρ = Density $[kg/m^3]$
ϕ = Generic thermo-chemical quantity
$\widetilde{\phi}$ = Favre-averaged value of ϕ
ϕ'' = Fluctuation of ϕ in the Favre-averaging process
$\widetilde{\phi''^2}$ = Variance of ϕ
$\overline{\phi}$ = Reynolds-averaged value of ϕ
ϕ' = Fluctuation of ϕ in the Reynolds-averaging process
Φ = Error function
χ = Scalar dissipation rate $[1/s]$
χ_{st} = Value of χ at stoichiometric conditions $[1/s]$
ω = Turbulent kinetic energy specific dissipation rate $[1/s]$

1. Introduction

The development of propulsion systems based on air-breathing engines for super-/hyper-sonic aircraft has fostered the study of supersonic combustion (e. g., see the review of Cecere et al. [1]). In these systems, hydrogen has advantages over other fuels because of its very short ignition delay time and high energy density. The investigation of hydrogen supersonic combustion presents significant difficulties and high costs for both experimental and numerical approaches. In fact, in supersonic combustion, the diffusion time scale becomes of the same order of magnitude as the time scale of the combustion reaction so that nonequilibrium effects may be relevant [2]. Moreover, high-Reynolds-number turbulent combustion is a formidable multi-scale problem, where the interaction between chemical kinetics, molecular, and turbulent transport occurs over a wide range of length and time scales. These features pose severe difficulties in the analysis and comprehension of the basic phenomena involved in supersonic combustion.
Concerning the numerical approach, in recent years, the need for efficient tools having affordable computational costs has driven the research towards: i) studying turbulent combustion in order to understand the interaction between turbulence and chemistry [3–6]; ii) improving kinetic schemes to describe the combustion process [7–9]. Higher accuracy can be achieved by employing models based on detailed kinetic mechanisms, but this usually leads to prohibitively expensive calculations. Therefore, reduced order models are often employed to condense the reaction mechanisms and cut down the computational costs [7]. Simplified approaches to combustion modelling have been proposed to further reduce the number of equations to be solved. These include: the reduction of the chemical scheme in intrinsic low dimensional manifolds (ILDM) [10]; flamelet-based approaches such as the flamelet-progress variable (FPV) [11] or flame prolongation of ILDM (FPI) [12]; and the flamelet generated manifolds approach (FGM) [13].

The present work is based on the FPV model for non-premixed flames. For this kind of combustion, the mixing process brings the reactants into the reaction layer so as to activate and sustain the combustion process [14]. The basic assumption of the flamelet model is that such a reactive-diffusive layer can be considered as an ensemble of small laminar flames, also known as flamelets. In the case of steady flows, the flame structure can be described as a function of the mixture fraction, Z, and of the progress parameter, Λ [15]. Standard steady state FPV models are built under the low Mach number hypothesis [16–19], computing the combustion process at a uniform given pressure. Obviously, in supersonic combustion, density variations due to the dynamics of the flow cannot be neglected. In the present work, the modified FPV

approach proposed by Oevermann [20, 21] is employed, in which the fluid temperature is not evaluated using the flamelet equation but is calculated by solving the full set of conservation equations for compressible flows including the energy balance equation. More recently, some authors have proposed an extension of FPV combustion models to compressible flows rescaling the source term of the progress variable equation and and employing a perturbation of the low-Mach-number flamelet solution [22, 23].

For turbulent combustion, a probability density function (PDF) is needed to compute the mean value and the variance of the thermo-chemical variables. The definition of such a PDF is critical since it has a strong impact on the solution. The aim of this work is to study the applicability of the statistically most likely distribution (SMLD) [24] approach to model the joint-PDF of Z and Λ in the case of supersonic combustion. The results obtained using the proposed model are validated versus experimental data and are compared with state-of-the-art numerical results available in the literature as well as with results obtained using the standard FPV model.

This work is organised as follow: sections 2 provides the theoretical description of the standard-FPV and FPV-SMLD models; section 3 provides the governing equations and some details of the numerical discretization. The analysis of the numerical results for the simulation of the NASA Langley Research Center supersonic hydrogen flame are presented in section 4 along with reference numerical and experimental data. Finally, some conclusions are provided.

2. The flamelet progress variable models

For the case of non-premixed combustion of interest here, the basic assumptions of the flamelet model are fulfilled for sufficiently large Damköhler number, Da. In fact, when the reaction layer thickness is very thin with respect to the Kolmogorov length scale, turbulent structures are unable to penetrate into the reaction zone and cannot destroy the laminar flame structure. Effects of turbulence only result in a deformation and straining of the flame surface and the flame structure can be described locally as a function of the mixture fraction, Z, the scalar dissipation rate, χ, and the time. The scalar dissipation rate, $\chi = 2D_Z(\nabla Z)^2$, is a measure of the mixing intensity representing the inverse of the characteristic diffusion time scale, D_Z being the diffusion coefficient of the mixture fraction. Therefore, the entire flame behaviour can be obtained as a combination of solutions of the laminar flamelet equation. In the present work, we consider a steady flamelet behaviour, so that chemical effects are entirely determined by the value of Z, whereas χ describes the effects of the flow on the flame structure according to the following steady laminar flamelet equation (SLFE) for the generic variable ϕ:

$$-\rho\frac{\chi}{2}\frac{\partial^2\phi}{\partial Z^2} = \dot{\omega}_\phi. \tag{1}$$

In equation (1), ρ is the density and $\dot{\omega}_\phi$ is the source term related to the variable ϕ [15]. In particular, the FPV model proposed by Pierce and Moin [11, 15] is employed to evaluate all of the thermo-chemical quantities involved in the combustion process. This approach is based on the parametrization of the generic thermo-chemical quantity, ϕ, in terms of the mixture fraction, Z, and of the progress parameter, Λ, instead of χ:

$$\phi = F_\phi(Z, \Lambda)\,. \tag{2}$$

Using such a parameter, independent of the mixture fraction, one can uniquely identify each flame state along the stable and unstable branches of the S-shaped curve. A suitable definition of Λ leads to a dramatic simplification of the presumed PDF closure model. On the other hand, the solution of the transport equation for Λ is quite complex since it requires non-trivial modelling of several unclosed terms [25]. In order to overcome such a difficulty, the progress parameter is derived from a reaction progress variable, C, such as the temperature or a linear combination of the main reaction products, whose behaviour is governed by a simpler transport equation. Therefore, a transport equation for C is solved and the flamelet library is parametrized in terms of Z and C. Requiring that the transformation between Λ and C be bijective, one has

$$\Lambda = F_C^{-1}(Z, C)\,, \tag{3}$$

and any thermo-chemical variable can be expressed as:

$$\phi = F_\phi(Z, F_C^{-1}(Z, C)) \,. \tag{4}$$

The choice of the progress variable is not unique and some recent works discuss in details this issue proposing a procedure for its optimal selection [26–28]. A suitable definition for the progress variable is the sum of the mass fractions of the main reaction products [26]; for hydrogen combustion [23]:

$$C = Y_{H_2O}. \tag{5}$$

A stretching with respect to the minimum and maximum conditional value of C given the mixture fraction is made, leading to the following form of the progress parameter:

$$\Lambda = \frac{C - C_{Min}|Z}{C_{Max}|Z - C_{Min}|Z} \,. \tag{6}$$

Equation (2) is taken as the solution of the SLFE (1). Cases in which there is not a unique mapping of this solution as a function of Z and Λ [11, 15] are excluded from the flamelet library, being very close to the equilibrium limit. Since flamelet libraries are computed in advance and are assumed to be independent of the flow field, one has to model the dependence of χ on Z [16, 29, 30]. In this work, the functional form of $\chi(Z)$ has been taken from the idealized flow configuration of counterflow diffusion flame [31] providing the following equation

$$\chi(Z) = \chi_{st} \frac{\Phi(Z)}{\Phi(Z_{st})}, \tag{7}$$

where Φ is the error function and χ_{st} and Z_{st} are evaluated at the stoichiometric point [31].

From equation (2) one can derive the generic thermo-chemical quantity ϕ. When a turbulence model is used, the Favre-averaged value of ϕ and its variance are computed as:

$$\widetilde{\phi} = \int\int F_\phi(Z, \Lambda) \widetilde{P}(Z, \Lambda) dZ d\Lambda, \tag{8}$$

$$\widetilde{\phi''^2} = \int\int (F_\phi(Z, \Lambda) - \widetilde{\phi})^2 \widetilde{P}(Z, \Lambda) dZ d\Lambda. \tag{9}$$

In the above equations, $\widetilde{P}(Z, \Lambda)$ is the density-weighted PDF,

$$\widetilde{P}(Z, \Lambda) = \frac{\rho P(Z, \Lambda)}{\overline{\rho}}, \tag{10}$$

$P(Z, \Lambda)$ is the joint PDF and $\overline{\rho}$ is the Reynolds-averaged density. Therefore, ϕ can be decomposed as

$$\phi = \widetilde{\phi} + \phi'', \qquad \widetilde{\phi} = \frac{\overline{\rho\phi}}{\overline{\rho}}, \tag{11}$$

and the density as

$$\rho \;\; = \;\; \overline{\rho} + \rho', \tag{12}$$

where ϕ'' and ρ' are the fluctuations. The joint-PDF, $\widetilde{P}(Z, \Lambda)$, plays a crucial role in the definition of the model, affecting both its accuracy and computational cost. Moreover, the choice of such a function is not straightforward because of the unknown statistical behaviour of the two variables Z and Λ [25], its definition being an open problem tackled by several research groups [32–35]. The aim of this work is to validate a model based on the statistically most likely distribution (SMLD) [24] for the joint PDF of Z and Λ [36]. The performance of the FPV-SMLD combustion model are assessed by computing a hydrogen-air supersonic flame, comparing the results with those obtained using the standard FPV model. The Reynolds-Averaged Navier–Stokes equations with k-ω turbulence closure [37] are solved and both the standard-FPV and the FPV-SMLD models employ the total energy conservation equation to evaluate the temperature field in order to improve the simulation of compressible reacting flows.

2.1. Presumed probability density function model

In this section, the standard FPV model [15] (called here model A) and the FPV-SMLD model (called here model B) [36] are briefly described.

The evaluation of the average quantities in equations (8) and (9) requires the PDF to be presumed. Employing the Bayes' theorem,

$$\widetilde{P}(Z,\Lambda) = \widetilde{P}(Z)\widetilde{P}(\Lambda|Z)\,, \tag{13}$$

one usually presumes the functional shape of the marginal PDF of Z and of the conditional PDF of $\Lambda|Z$. In model A, statistical independence between Z and Λ is assumed, so that $\widetilde{P}(Z,\Lambda) = \widetilde{P}(Z)\widetilde{P}(\Lambda)$. Furthermore, the statistical behaviour of the mixture fraction is described by a β-distribution. In fact, it has been shown by several authors that the mixture fraction behaves like a passive scalar whose statistical distribution can be approximated by a β function [38–40]. The two-parameter family of the β-distribution for the variable $x \in [0,1]$ is given by:

$$\beta(x;\widetilde{x},\widetilde{x''^2}) = x^{a-1}(1-x)^{b-1}\frac{\Gamma(a+b)}{\Gamma(a)\Gamma(b)}, \tag{14}$$

where $\Gamma(x)$ is the Euler function and a and b are two parameters related to $\widetilde{x}$ and $\widetilde{x''^2}$

$$a = \frac{\widetilde{x}(\widetilde{x}-\widetilde{x}^2-\widetilde{x''^2})}{\widetilde{x''^2}}, \quad b = \frac{(1-\widetilde{x})(\widetilde{x}-\widetilde{x}^2-\widetilde{x''^2})}{\widetilde{x''^2}}. \tag{15}$$

Finally, model A employs a Dirac distribution for $\widetilde{P}(\Lambda)$, leading to a great simplification in the theoretical procedure. With these assumptions, the Favre-average of a generic thermo-chemical quantity is given by:

$$\widetilde{\phi} = \int\int F_\phi(Z,\Lambda)\widetilde{\beta}(Z)\delta(\Lambda-\widetilde{\Lambda})dZdC = \int F_\phi(Z,\widetilde{\Lambda})\widetilde{\beta}(Z)dZ. \tag{16}$$

Therefore, in addition to the standard RANS equations, one has to solve only three transport equations (for $\widetilde{Z}$, $\widetilde{Z''^2}$ and $\widetilde{C}$) to evaluate all of the thermo-chemical quantities, thus avoiding the expensive solution of one transport equation for each chemical species. Model B, employing the SMLD approach for the joint PDF, does not need any assumption about the form of $\widetilde{P}(Z,\Lambda)$. Following such an approach, the probability distribution is evaluated as a function of an arbitrary number of moments of Z and Λ. It is noteworthy that, even though equation (1) is based on the assumption that Z and Λ are independent, one can properly take into account the statistical correlation between Z and Λ employing the SMLD joint-PDF in the evaluation of the effects of turbulence [32].

In this work, the first two moments of the joint probability density function $\widetilde{P}(\vec{x})$, where $\vec{x} = (Z,\Lambda)^T$, are assumed to be known; therefore, the joint-PDF reads [36] :

$$\begin{aligned}\widetilde{P}_{SML,2}(Z,\Lambda) = \frac{1}{\mu_0}\exp\Big\{&-\Big[\mu_{1,1}(Z-\widetilde{Z})+\mu_{1,2}(\Lambda-\widetilde{\Lambda})\Big]\\ &-\frac{1}{2}\Big[\mu_{2,11}(Z-\widetilde{Z})^2+\mu_{2,12}(Z-\widetilde{Z})(\Lambda-\widetilde{\Lambda})+\mu_{2,21}(\Lambda-\widetilde{\Lambda})(Z-\widetilde{Z})+\mu_{2,22}(\Lambda-\widetilde{\Lambda})^2\Big]\Big\}.\end{aligned} \tag{17}$$

In the equation above, μ_0 is a scalar, $\vec{\mu_1}$ is a two - component vector, and $\overleftrightarrow{\mu_2}$ is a square matrix of rank two:

$$\mu_0 = \int d\vec{x}\widetilde{P}_{SML,2}(\vec{x}), \tag{18}$$

$$-\mu_{1,i} = \int d\vec{x}\partial_{x_i}\widetilde{P}_{SML,2}(\vec{x}) = \beta(1;\widetilde{\xi}_i,\widetilde{\xi_i''^2}) - \beta(0;\widetilde{\xi}_i,\widetilde{\xi_i''^2}), \tag{19}$$

$$\delta_{kl} - \mu_{2,kn}\,\widetilde{\xi_n'\xi_l'} = \int d\vec{x}\partial_{x_k}((x_l-\widetilde{\xi}_l)\widetilde{P}_{SML,2}(\vec{x})) = \beta(1;\widetilde{\xi}_k,\widetilde{\xi_k'\xi_l'}) - \widetilde{\xi}_k\mu_{1,l}, \tag{20}$$

where i, k, n, and l indicate the vector components; $\widetilde{\xi}_i$, $\widetilde{\xi_i'}$ and $\widetilde{\xi_i''^2}$ are the mean ($\widetilde{x_i}$), the fluctuation ($x_i-\widetilde{x_i}$) and the variance ($\widetilde{x_i''^2}$) of the i-th component of $\vec{x}$, respectively; finally, β indicates the beta distribution function. Using model B, one has to solve four additional transport equations (for $\widetilde{Z}$, $\widetilde{Z''^2}$, $\widetilde{C}$, and $\widetilde{C''^2}$) to evaluate all of the thermo-chemical quantities.

3. Governing equations

3.1. Flow equations

The governing equations for an axisymmetric multi-component reacting compressible flow can be written as:

$$\partial_t \vec{Q} + \partial_x(\vec{E} - \vec{E}_\nu) + \partial_y(\vec{F} - \vec{F}_\nu) = \vec{S}, \tag{21}$$

where t is the time; x and y are the axial and the radial coordinate, respectively; $\vec{Q}$=$(\overline{\rho}, \overline{\rho}\widetilde{u}_x, \overline{\rho}\widetilde{u}_y, \overline{\rho}\widetilde{H} - \widetilde{p}_t, \overline{\rho}\widetilde{k}$, $\overline{\rho}\widetilde{\omega}, \overline{\rho}\widetilde{R}_n)$ is the vector of the conservative variables; $\vec{E}$, $\vec{F}$, and $\vec{E}_v$, $\vec{F}_v$ are the inviscid and viscous flux vectors [41], respectively; $\vec{S}$ is the vector of the source terms; $\overline{\rho}$, $(\widetilde{u}_x, \widetilde{u}_y)$, $\widetilde{H}$ indicate the Reynolds-averaged value of density, the Favre-averaged values of velocity components, and the specific total enthalpy given by $\widetilde{H} = \widetilde{h} + \frac{1}{2}(\widetilde{u}_x^2 + \widetilde{u}_y^2) + \frac{5}{3}\widetilde{k}$, $\widetilde{h}$ being the specific enthalpy; $\widetilde{p}_t = \widetilde{p} + \frac{2}{3}\widetilde{k}$, $\widetilde{p}$ being the Favre-averaged value of pressure; $\widetilde{k}$ and $\widetilde{\omega}$ are the Favre-averaged values of the turbulence kinetic energy and of its specific dissipation rate; $\widetilde{R}_n$ is a generic set of conserved variables related to the combustion model. In this framework, $\widetilde{R}_n$ is the set of variables of the flamelet model, namely, $\widetilde{Z}$, $\widetilde{Z''^2}$, $\widetilde{C}$, $\widetilde{C''^2}$ (see the following subsection).
The heat flux in the total energy equation, namely,

$$q = -\rho c_p D_T \nabla T + \sum_{n=1}^{N_s} \rho V_n Y_n h_n + \dot{q}_{react}, \tag{22}$$

is composed of three terms since the Dufour effect is neglected; D_T is the thermal diffusivity, c_p the specific heat at constant pressure. The mass diffusion term is modelled by the Fick law considering $V_n = -D\frac{\nabla Y_n}{Y_n}$, assigning mixture diffusivity, D, to each species with the assumption of Lewis number equal to one [14]. The third term at the right hand side of equation (22) represents the heat release rate:

$$\dot{q}_{react} = \sum_{k=1}^{N} \Delta h^o_{f,k} \dot{\omega}_k \,, \tag{23}$$

where $\Delta h^o_{f,k}$ is the mass formation enthalpy and $\dot{\omega}_k$ is the production rate of species k.

3.2. Turbulent FPV transport equations

For the case of turbulent flames, the solution of the SLFE (2) is expressed in terms of the Favre averaged values of Z and C and of their variance. Using model A, one can tabulate all chemical quantities in terms of $\widetilde{Z}$, $\widetilde{Z''^2}$ and $\widetilde{C}$, since, due to the properties of the δ-distribution, the model is independent of $\widetilde{C''^2}$. On the other hand, model B expresses ϕ also in terms of $\widetilde{C''^2}$ and therefore an additional transport equation needs to be solved. In this case, the transport equations for the combustion model (included in equation (21)) are written as:

$$\partial_t(\overline{\rho}\widetilde{Z}) + \vec{\nabla}\cdot(\overline{\rho}\widetilde{\vec{u}}\widetilde{Z}) = \vec{\nabla}\cdot\left[(D + D^t_{\widetilde{Z}})\overline{\rho}\vec{\nabla}\widetilde{Z}\right], \tag{24}$$

$$\partial_t(\overline{\rho}\widetilde{Z''^2}) + \vec{\nabla}\cdot(\overline{\rho}\widetilde{\vec{u}}\widetilde{Z''^2}) = \vec{\nabla}\cdot\left[(D + D^t_{\widetilde{Z''^2}})\overline{\rho}\vec{\nabla}\widetilde{Z''^2}\right] - \overline{\rho}\widetilde{\chi} + 2\overline{\rho}D^t_{\widetilde{Z}}(\vec{\nabla}\widetilde{Z})^2, \tag{25}$$

$$\partial_t(\overline{\rho}\widetilde{C}) + \vec{\nabla}\cdot(\overline{\rho}\widetilde{\vec{u}}\widetilde{C}) = \vec{\nabla}\cdot\left[(D + D^t_{\widetilde{C}})\overline{\rho}\vec{\nabla}\widetilde{C}\right] + \overline{\rho}\overline{\dot{\omega}_C}, \tag{26}$$

$$\partial_t(\overline{\rho}\widetilde{C''^2}) + \vec{\nabla}\cdot(\overline{\rho}\widetilde{\vec{u}}\widetilde{C''^2}) = \vec{\nabla}\cdot\left[(D + D^t_{\widetilde{C''^2}})\overline{\rho}\vec{\nabla}\widetilde{C''^2}\right] - \overline{\rho}\widetilde{\chi}_C + 2\overline{\rho}D^t_{\widetilde{C}}(\vec{\nabla}\widetilde{C})^2 + 2\overline{\rho}\widetilde{C''\dot{\omega}''_C}, \tag{27}$$

where $\widetilde{\chi}_C$ is modelled in terms of $\widetilde{Z''^2}$ and $\widetilde{C''^2}$ [33], namely $\widetilde{\chi}_C = \frac{\widetilde{Z''^2}\widetilde{\chi}}{\widetilde{C''^2}}$, $D = \nu/Pr$ is the diffusion coefficient for all of the species; ν and Pr are the kinematic viscosity and the Prandtl number, respectively; $D^t_{\widetilde{Z}} = D^t_{\widetilde{Z''^2}} = D^t_{\widetilde{C}} = D^t_{\widetilde{C''^2}} = \nu_t/Sc_t$ are the turbulent mass diffusion coefficients, Sc_t being the turbulent Schmidt number equal to 0.8; finally, $\dot{\omega}_C$ is the source term for the progress variable precomputed and tabulated in the flamelet library. At every iteration, the values of the flamelet variables are updated

using equations (24)-(27) and the Favre-averaged thermo-chemical quantities are computed, using equation (8). Such solutions provide the mean mass fractions which are used to evaluate all of the transport properties of the fluid, namely the molecular viscosity, the thermal conductivity and the species diffusion coefficient. The flamelet library has been generated using the detailed kinetic scheme proposed by Saxena and Williams [42], with 244 sub-reactions upon 50 species, over a grid with 250 uniformly distributed points in the $\widetilde{Z}$ and $\widetilde{C}$ directions, and 50 uniformly distributed points in the $\widetilde{Z''^2}$ and $\widetilde{C''^2}$ directions. A constant background pressure equal to 100 kPa has been considered and the boundary values for Z and C correspond to the conditions of the air and H_2 streams, namely: $\widetilde{Z} = 0$ and $\widetilde{C} = 0$ for the air stream; and $\widetilde{Z} = 1$ and $\widetilde{C} = 0$ for the fuel jet. The solution of the SLFE has been obtained by using the FlameMaster code [43] and a quadri-linear interpolation scheme is employed to extract the data from the library.

3.3. Numerical scheme and boundary conditions

The numerical method developed in [37] has been employed to solve the steady-state RANS equations with k-ω turbulence closure. A cell-centred finite volume numerical scheme is used, the computational domain being discretized by a multi-block structured mesh. The convective and viscous terms are discretized by the third-order-accurate Steger and Warming [44] flux-vector-splitting scheme and by second-order-accurate central differences, respectively. An implicit time marching approach is used with a factorization based on the diagonalization procedure of Pulliamm and Chaussee [45], employing a scalar alternating direction implicit (ADI) solution procedure [46]. In the present work, only steady flows are considered; therefore, the ADI scheme is iterated in the pseudo-time until a residual drop of at least five orders of magnitude for all of the conservation-law equations (21) is achieved. Characteristic boundary conditions for the flow variables are imposed at inflow and outflow points. In particular, a plug flow is imposed at the inlet points of the computational domain so as to match the experimental conditions at the inlet section of the chamber (see table 1). Moreover, k, ω, and R_n are assigned at inflow points, whereas they are linearly extrapolated at outflow points. No slip and adiabatic conditions are imposed at walls, where k is set to zero and ω is evaluated as proposed in [47]:

$$\omega = 60\,\frac{\nu}{0.09\,y_{n,1}^2}, \tag{28}$$

where $y_{n,1}$ is the distance of the first cell center from the wall; the homogeneous Neumann boundary condition is used for R_n (non-catalytic wall). Finally, symmetry conditions are imposed on the axis.

4. Results and discussion

4.1. Description of the test case

The hydrogen-air supersonic combustion burner studied by Cheng et al. [48] at the NASA Langley Research Center has been considered as a suitable test case for validating the proposed FPV-SMLD combustion model in supersonic flow conditions. At the inlet section of the chamber, the supersonic flow (see figure 1) is characterized by an annular axisymmetric jet of hot vitiated wet air at Mach number equal to 2, average axial velocity of 1420 m/s, temperature of 1250 K and pressure of 107 kPa. The values of the inner and outer diameters of the vitiated air annular duct are equal to 3.812 mm and 17.78 mm, respectively. The vitiated air composition ($Y_{O_2} = 0.201$, $Y_{H_2O} = 0.255$ and $Y_{N_2} = 0.544$) is obtained by a pre-combustion at low temperature [48]. The diameter of the fuel stream is $d_{ref} = 2.362$ mm, taken as the reference length. The hydrogen flow is estimated to be chocked with average axial velocity of 1780 m/s, temperature of 545 K, and pressure of 112 kPa. The operating conditions reported by Cheng et al. [48] are summarized in table 1 together with the turbulent intensity levels, Tu_{in}, and the turbulent viscosity, $\nu_{T_{in}}$, at the inlet section. The computational domain, shown in figure 2, is axisymmetric and includes the divergent part of the air nozzle, necessary to recover the correct flow quantities at the inlet section of the chamber; it extends 150 d_{ref} and 50 d_{ref} in the axial and radial directions, respectively, and, after a grid refinement study, has been discretized using about 100000 cells. The characteristic cell lengths at the exit of the divergent part of the nozzle are about 0.13 mm and 0.05 mm in the axial and radial directions, respectively. Numerical results obtained using the two models described in the previous sections are discussed and validated versus the

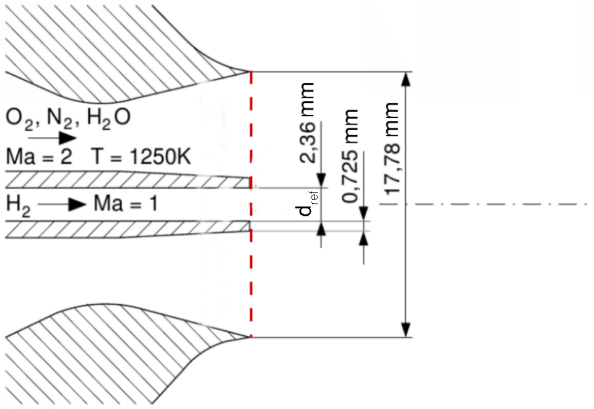

Figure 1: Schematic of the Cheng's Flame burner. The red-dashed line represents the exit section of the burner and so the inlet section of the chamber.

experimental data of Cheng et al. [48] and the numerical results available in the literature [7, 49]. Moreover, a detailed analysis of the flame structure is provided.

Table 1: Parameters for the simulation of the Cheng's combustion chamber [48].

	Ma	u(m/s)	T (K)	p (kPa)	Y_{H_2}	Y_{O_2}	Y_{H_2O}	Y_{N_2}	Tu_{in}	$\nu_{T_{in}}(m^2/s)$
H_2 jet	1	1780	545	112	1	0	0	0	5.78%	0.00023
Air stream	2	1420	1250	107	0	0.201	0.255	0.544	10.24%	0.00034

4.2. Comparison between numerical and experimental data

Figure 3 provides the Mach number contours obtained using model A (left panels) and model B (right panels). The close-up view of the near-burner region (bottom panels) indicates that the inlet Mach number value matches the experimental data for both computations. The distributions of the streamwise component of the velocity, u, at several abscissae along the chamber are shown in figure 4. A good agreement with the experimental data [48] is obtained for both models. Figure 5 (top frame) shows a qualitative comparison between the temperature contours evaluated with the two models. It appears that the computed flame shapes are quite different. Model A predicts a reaction zone attached to the burner, whereas model B correctly predicts the flame lift-off. In the bottom frame of figure 5 one can find the two corresponding progress-variable contour plots. The solution obtained using model A provides non-zero values of the progress variable in the region close to the burner, indicating that the reaction is active. Figure 6 presents the temperature field obtained using model A (left panel) and model B (right panel) in comparison with the results of an accurate LES by Boivin et al. [7]. One can observe that model B predicts the lift-off height, evaluated as the position of maximum temperature gradient, at about $x = 26\ d_{ref}$, whereas model A predicts an height of about 9 d_{ref}. The results by Boivin et al. [7], used as reference, predict a lift-off height equal to 25 d_{ref}. For both models, the jet shape and the aperture of the flame at $x/d_{ref} = 50$, equal about to 10 d_{ref}, are in good agreement with the experimental data (not shown). For a quantitative analysis of the results, figures 7–9 provide the comparison among the results obtained using the two FPV models, the numerical results provided in references [7, 49], and the experimental data [48]. Figure 7 shows the distribution of the main thermo-chemical quantities along the axis of the burner. The evaluation of the $\widetilde{Z}$ and $\widetilde{Z''^2}$ are very slightly improved by model B; a reasonable improvement of the prediction of the distribution of OH mass fraction is also obtained; whereas, H_2 and H_2O mass fractions are quite well predicted in comparison with model A. It appears that model A is not able to reproduce the correct flame core structure, providing a

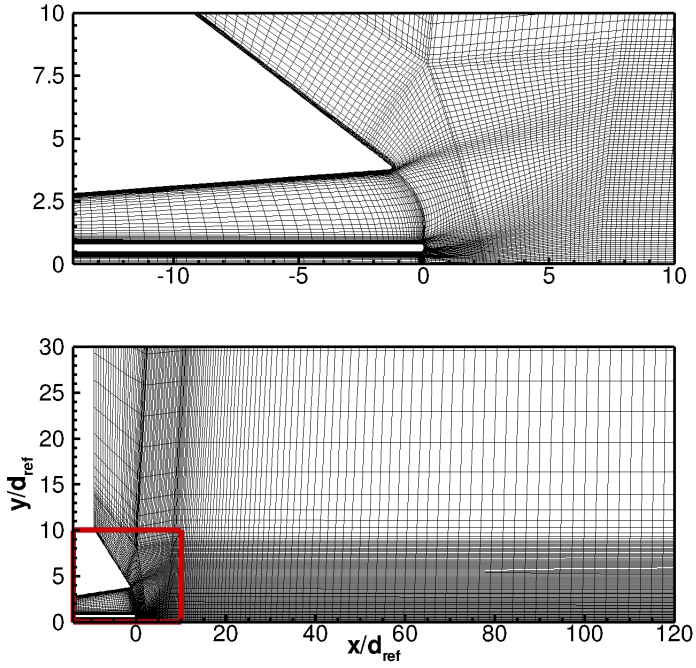

Figure 2: Computational domain discretization (lower frame) and a detail of the injectors (upper frame).

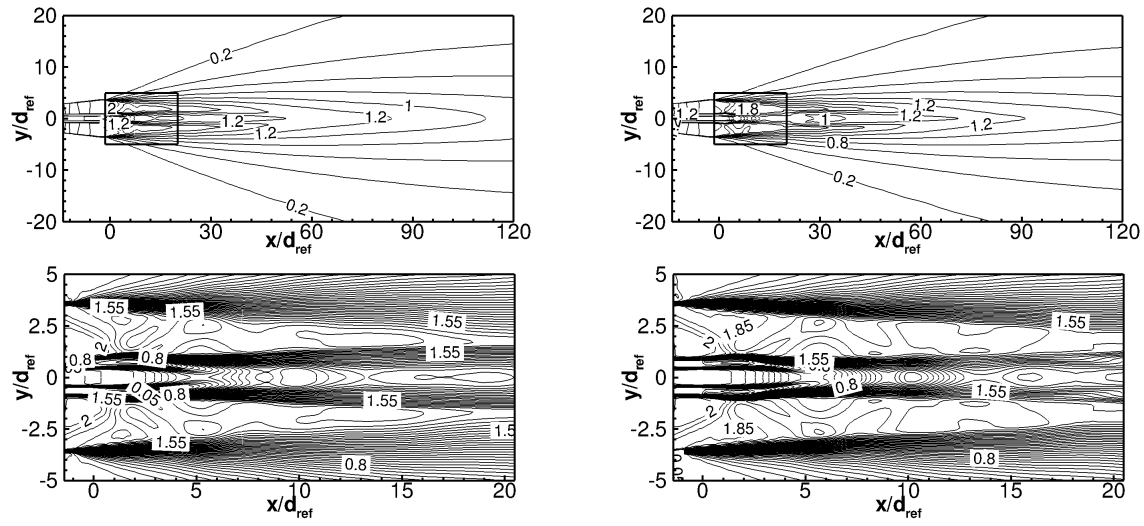

(a) Model A

(b) Model B

Figure 3: Mach number contours obtained with model A (left) and model B (right), with a close up of the near-burner region (bottom).

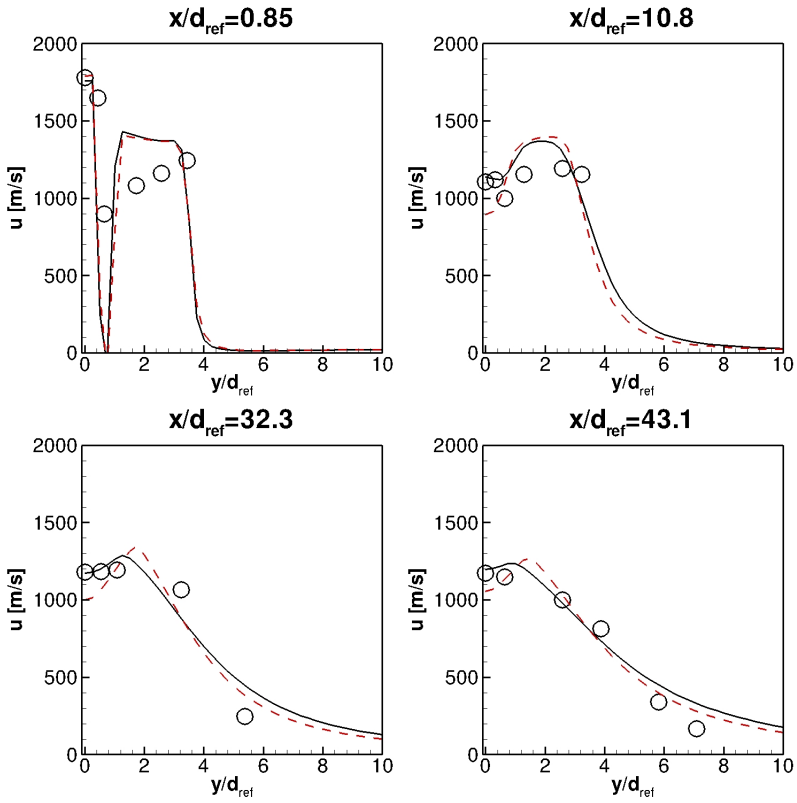

Figure 4: Stream-wise velocity distributions at several radial sections: model A, red dashed line; model B, black solid line; symbols, experimental data.

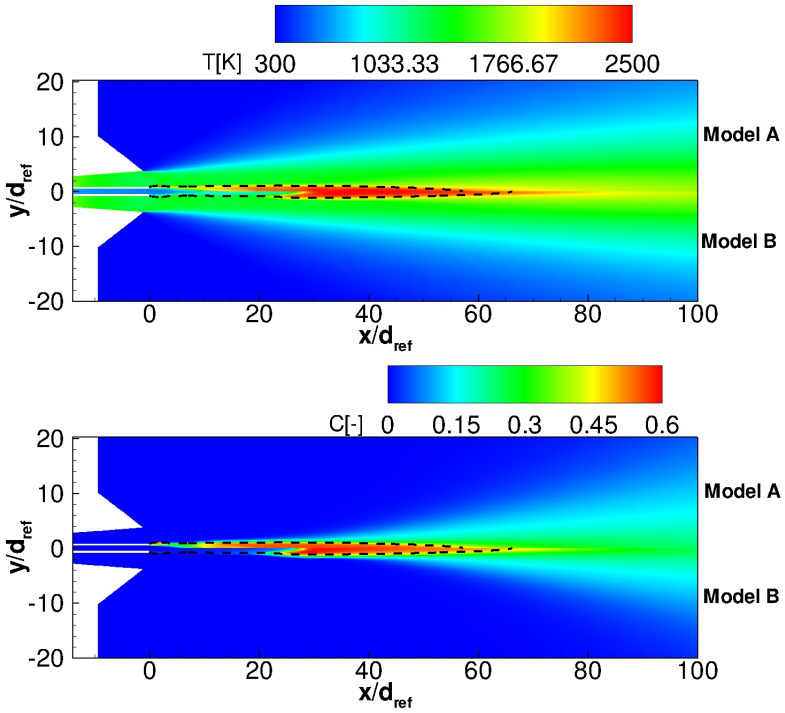

Figure 5: Temperature (top) and progress variable (bottom) contours for the Cheng's combustion chamber with the Z_{st} iso-line superimposed (black dashed line).

too high reaction rate as soon as the two streams (H_2–wet-air) start to mix. As a consequence, model A predicts Y_{H_2O} maximum at about 10 x/d_{ref}, as shown in the middle right frame of figure 7. On the other hand, model B can reproduce the ignition spatial delay with a strong increase of the temperature at about $x/d_{ref} = 30$ (figure 7 middle-left frame).

Figure 7 also provides the numerical results obtained using an LES by Boivin et al. [7], for comparison; they appear to be in good agreement with the results obtained by model B, confirming the good level of accuracy achieved by such a model. Analysing the temperature and water-mass-fraction experimental distributions shown in figure 7, one can notice that the temperature begins to decrease at $x/d_{ref} = 50$ whereas the water mass fraction increases up to about $x/d_{ref} = 65$. This is due to the entrainment of the surrounding unburned air into the flame, which induces an increase of the mass flow rate and allows the reactions to occur even if the flame cannot heat up the surrounding flow. In particular, model A predicts an early increase of the temperature and of the water mass fraction, due to the heat being released very close to the burner. As a consequence, the entrainment of the surrounding unburned air into the flame is strongly overestimated using such a model with respect to model B. The entrainment can be evaluated by computing the total mass flow rate through the inlet of the chamber, at $x/d_{ref} = 0$, and at the sections $x/d_{ref} = 25$ and $x/d_{ref} = 50$. Due to the axial-symmetry, the effective surfaces intersected by the flow can be estimated as the circles with radius equal to the maximum extension of the temperature profiles, namely $(y/d_{ref})_0 = 5.540$, $(y/d_{ref})_{25} = 16.02$, and $(y/d_{ref})_{50} = 27.115$ (see figure 8). The mass fluxes computed by model B are equal to $\dot{m}_{x/d_{ref}=0} = 96.28\ g/s$, $\dot{m}_{x/d_{ref}=25} = 511.78\ g/s$, and $\dot{m}_{x/d_{ref}=50} = 1163.77\ g/s$, respectively. Model A clearly predicts different values of the mass fluxes at the same locations: $\dot{m}_{x/d_{ref}=0} = 98.07\ g/s$, $\dot{m}_{x/d_{ref}=25} = 681.83\ g/s$, and $\dot{m}_{x/d_{ref}=50} = 1202.08\ g/s$.

Figure 9 shows the distribution of some relevant thermo-chemical variables at several abscissae along the chamber axis, providing a comparison among the results obtained by the two FPV models, an LES using a reduced-chemistry combustion model [7], a mixture-fraction based model [49], and experimental

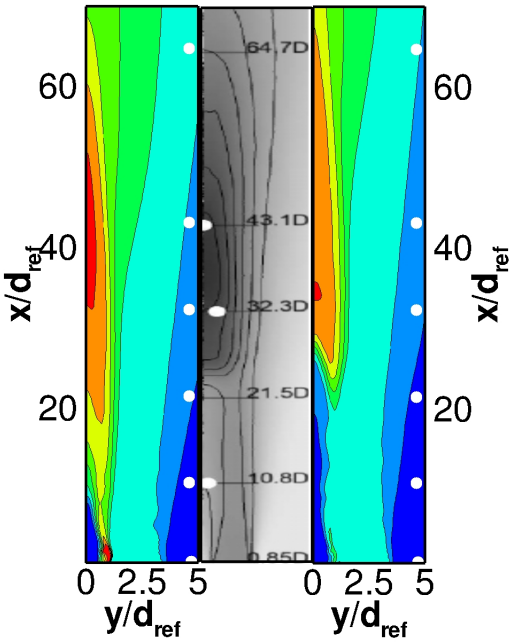

Figure 6: Comparison between the temperature contours computed by model A (left), Boivin et al. [7] (center), model B (right). The contour lines are plotted from $1000K$ to $2500K$ with step equal to $250K$.

results [48]. The H_2 and O_2 mass fraction distributions agree fairly well with LES and experimental data. The improvement with respect to the results of model A is more evident in the near axis region. Model A predicts a thin reacting zone near the burner, so that at $x/d_{ref} = 0.85$ (see figure 8) and $x/d_{ref} = 10.8$ (see figure 9) the temperature distributions present a spike close to the axis. This spike characterizes also the water mass-fraction distribution of the mixture-fraction-based model by Thibault and Boivin [49]. Instead, model B is not affected by this problem and correctly predicts the flame core.

4.3. The flame structure

Following the work of Moule et al. [50] and of Boivin et al. [7] on the present supersonic burner, we provide a detailed analysis of the flame structure. Moule et al. [50] identify three characteristic regions of the flame, namely: 1) the auto-ignition zone, $10 \leq x/d_{ref} \leq 18$, where the mixture prepares to ignite; 2) the stabilization region, $18 \leq x/d_{ref} \leq 26$, where the flame starts; 3) the combustion region, $30 \leq x/d_{ref} \leq 40$.

In the first zone, the initial steps of the hydrogen oxidation take place and the reaction produces simple radicals. For hydrogen combustion, the hydroperoxyl radical HO_2 can be considered as a good marker of autoignition; however, since the HO_2 concentration also increases in fuel-rich reaction zones of ignited mixtures, Boivin et al. [7] proposed a more accurate criterion for detecting autoignition. Such a criterion requires the simultaneous presence of high values of the normalized production rate of HO_2 and of the reactivity of the mixture, λ, defined as the positive eigenvalue of the Jacobian of the chemical source term associated to the autoignition chain-branching reaction [7]. For the present supersonic lift-off flame, the results of the LESs discussed in references [50] and [7] confirm that using this approach it is possible to identify accurately the autoignition region as well as the consecutive transition to the stabilization region characterized by the HO_2 depletion.

Analysing the results of the present RANS simulations, we can show that model B can provide a flame structure corresponding to that described above. Figure 10 shows the contours of the HO_2 production rate,

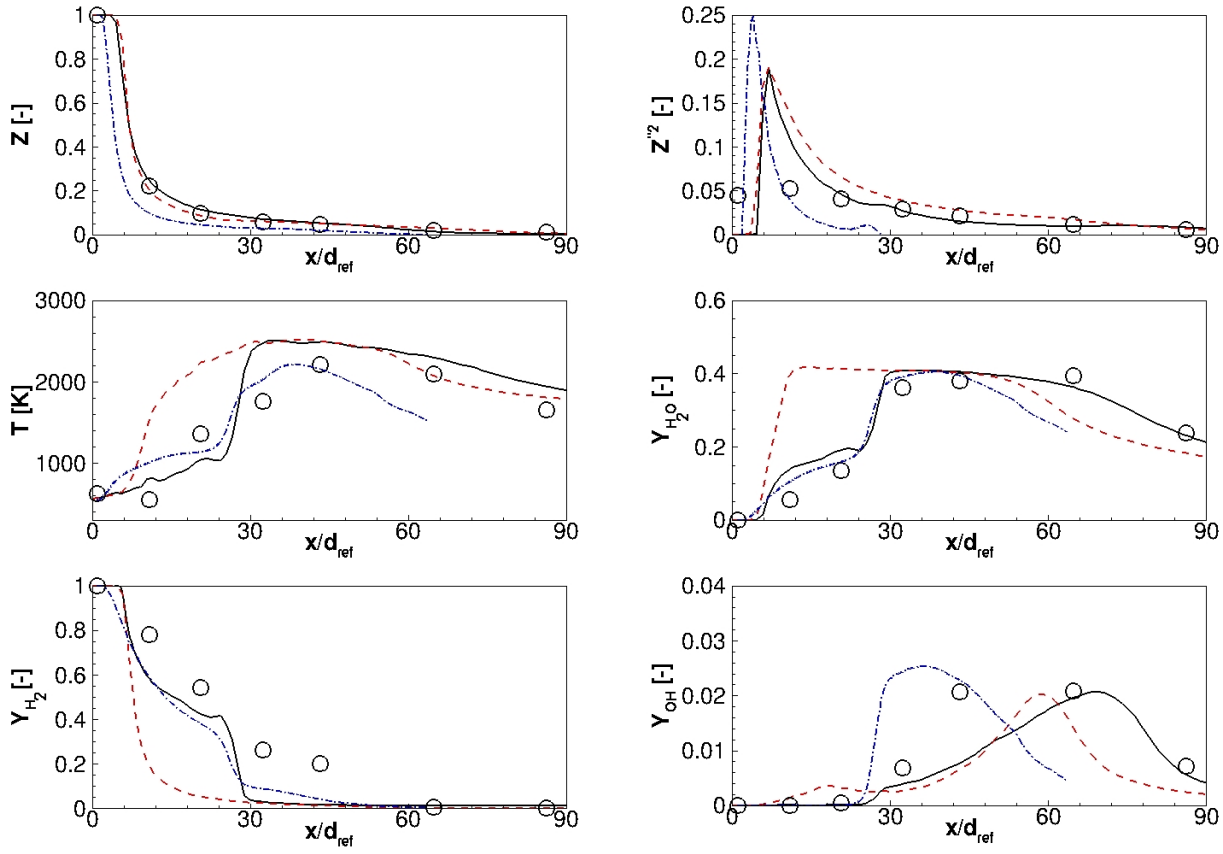

Figure 7: Distributions of different thermo-chemical quantities along the axis ($y/d_{ref} = 0$). Model A, red dashed line; model B, solid black line; Boivin et al. dashed-dotted blue line [7]; symbols, experimental data [48].

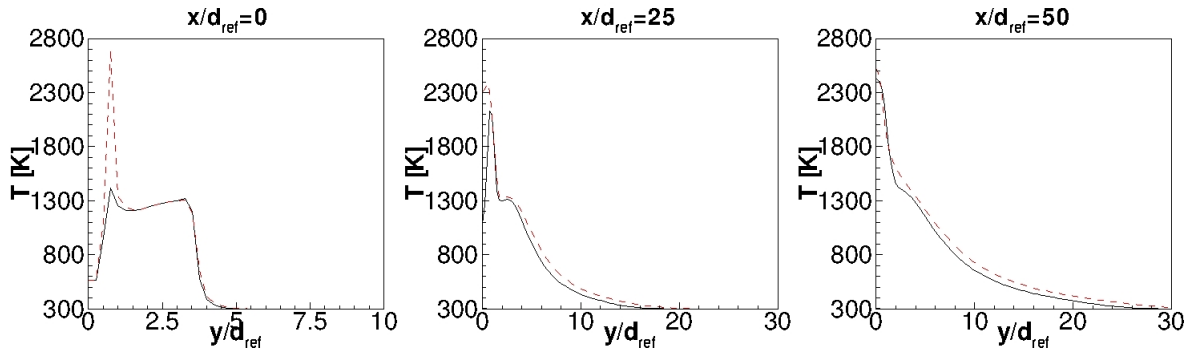

Figure 8: Temperature distributions at $x/d_{ref} = 0$, $x/d_{ref} = 25$, and $x/d_{ref} = 50$: model A, red dashed line; model B, solid black line.

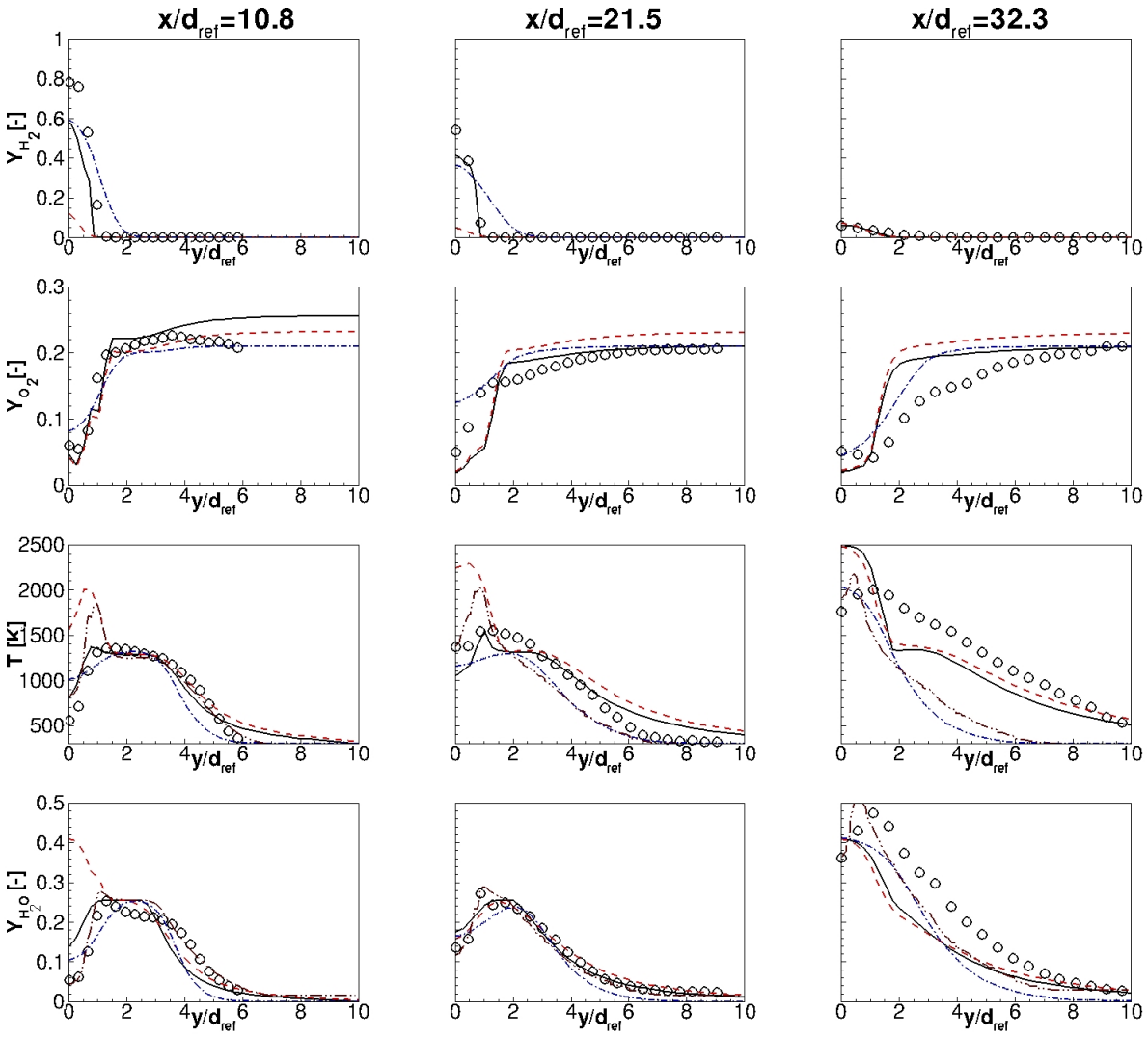

Figure 9: Chemical species distributions at $x/d_{ref} = 10.8$, $x/d_{ref} = 21.5$, and $x/d_{ref} = 32.3$: model A, red dashed line; model B, solid black line; Boivin et al. dashed-dotted blue line [7]; Thibault and Boivin dashed-dotted-dotted brown line [49]; symbols, experimental data [48].

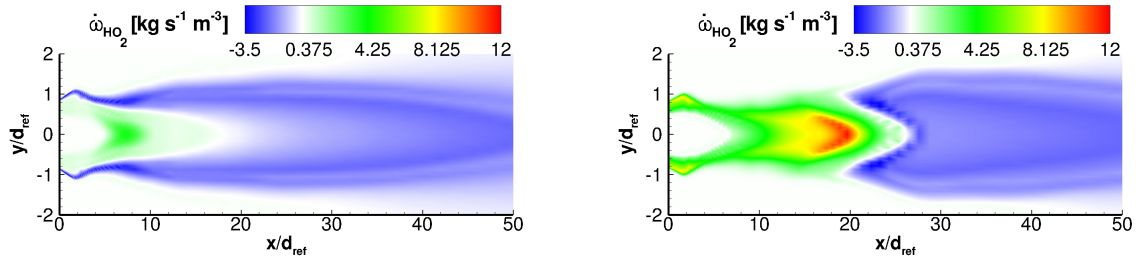

(a) Model A (b) Model B

Figure 10: Model A and Model B solutions: contours of $\dot{\omega}_{HO_2}$.

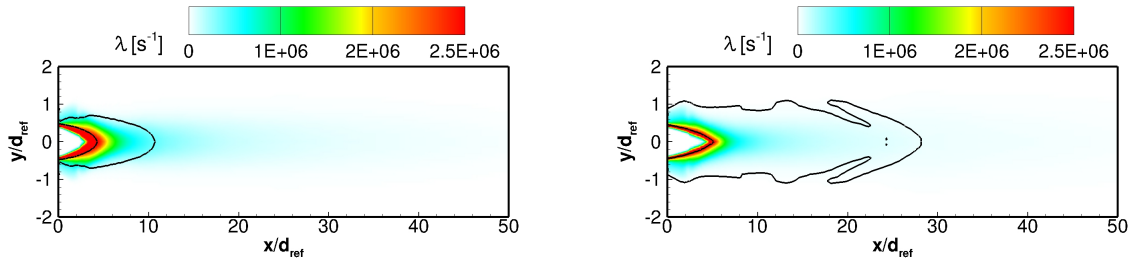

(a) Model A (b) Model B

Figure 11: Model A and Model B solutions: reactivity contour plot with the Y_{HO_2} iso-line $[3 \times 10^{-5}]$ superimposed.

$\dot{\omega}_{HO2}$, computed using model A (left) and model B (right). This figure indicates that both models predict a substantial HO_2 production downstream of the jet exit, in agreement with the results of the LES by Moule et al. [50] (see figure 17 of their paper). Moreover, it appears that the production region is followed by depletion taking place in the stabilization region. Figure 11 shows the contour plot of λ together with the $Y_{HO_2} = 3 \times 10^{-5}$ iso-line, considered as the reference value for high-temperature hydrogen autoignition [50]. It appears that the most reactive part of mixture is in the near-burner zone, where the mixing among the reactants is stronger. Both models properly evaluate the reactivity, in good agreement with the results of the LES of Moule et al. [50] (see figure 19 therein). Looking at the contours of $\dot{\omega}_{HO2}$ in figure 10 and at the contours of λ in figure 11, one can verify the conjecture of Boivin et al. concerning the autoignition region. In fact, model B predicts the autoignition at $7 \leq x/d_{ref} \leq 23$, where sufficiently high values of the reactivity and of the HO_2 production rate are achieved. On the other hand, model A predicts a too fast reaction rate, providing a shorter autoignition region for $3 \leq x/d_{ref} \leq 11$.

In the second zone, the flame finds its stable position and, as shown in figure 12, it is characterized by high values of the heat release rate. Figure 12 also shows the sonic iso-line and the axial temperature profile superposed to the contours of the heat release rate. According to the LES results of Moule et al. [50], although the highest temperature occurs in the subsonic region, $32 \leq x/d_{ref} \leq 38$, high values of $\dot{q}_{react}$ are concentrated in the neighbourhood of the stabilization region of the flame, $18 \leq x/d_{ref} \leq 26$. For the present RANS computations, model A predicts high values of the temperature and of the heat release too close to the burner, whereas, model B provides results in very good agreement with the LES concerning both the heat release region and the temperature profile along the axis of the burner.

As proposed by Boivin et al. [7], it is also possible to employ a unique parameter that identifies the

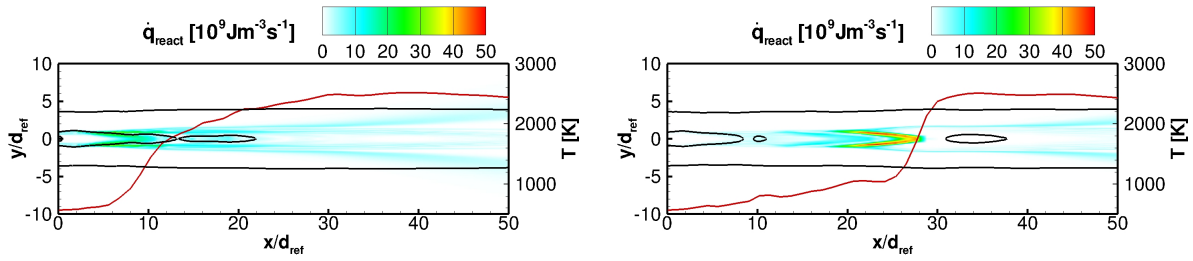

(a) Model A (b) Model B

Figure 12: Model A and Model B solutions: heat reaction rate contour plot with the $Ma = 1$ iso-line (black solid line) and the axial temperature profile (red solid line) superimposed.

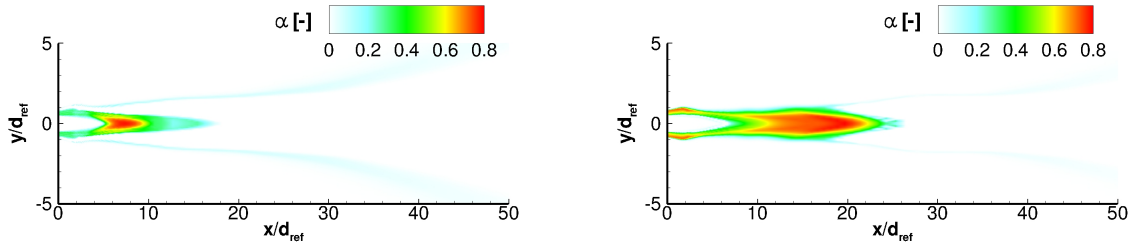

(a) Model A (b) Model B

Figure 13: Model A and Model B solutions: contour plot of α.

occurrence of autoignition, namely,

$$\alpha = \frac{\dot{\omega}^{+}_{HO_2} - \dot{\omega}^{-}_{HO_2}}{\dot{\omega}^{+}_{HO_2}}\,, \tag{29}$$

$\dot{\omega}^{+/-}_{HO_2}$ indicating the positive/negative part of $\dot{\omega}_{HO_2}$ and representing the production and the destruction rates of HO_2, respectively. According to Boivin et al. [7], the autoignition occurs when α decreases from its maximum reference value ($\alpha_{max} \approx 0.95$) to its minimum reference value ($\alpha_{min} \approx 0.05$). Figure 13 a) and b) show the α contour plots obtained by model A and B, respectively, confirming that model B is capable of predicting the transition from the autoignition to the stabilization region at about 27 d_{ref}, providing a good estimate of the lift-off height.

Finally, figure 14 shows that in the third region ($30 \leq x/d_{ref} \leq 40$) the combustion develops and is characterized by high values of OH production rate.

4.4. Z and Λ distributions

In this section, we focus on the analysis of the flow regions where large differences between the predictions of models A and B are observed. In particular, we compare the $\widetilde{P}_{SML,2}$ joint distribution with the $\beta-$distribution for Z and with the $\delta-$function for Λ at three points: two of them are on the axis ($y/d_{ref} = 0$) and are taken close to the lift-off heights evaluated with the two models, $x/d_{ref} = 8$ and $x/d_{ref} = 27$, respectively; the third point is close to the jet exit ($x/d_{ref} = 0.85$, $y/d_{ref} = 0.8$), where a spurious temperature peak is predicted by model A (see figures 8). All the distributions are computed using the values of the mean and variance obtained by model B.

The first point ($x/d_{ref} = 8$) is in the stabilization region for the solution obtained by model A and falls in the mixing non-burning region for the solution obtained by model B. This is clearly indicated by the

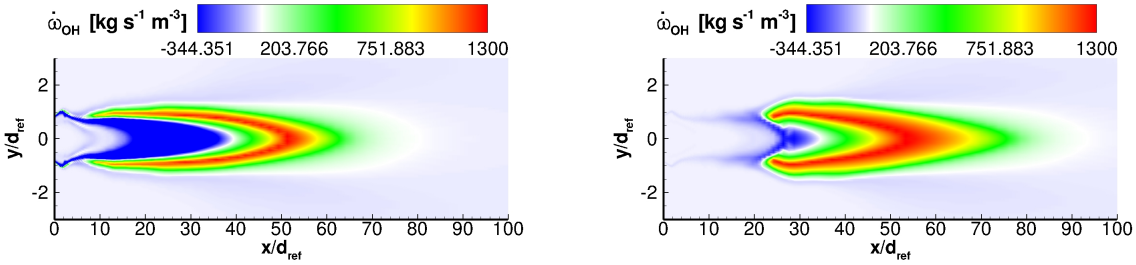

(a) Model A (b) Model B

Figure 14: Model A and Model B solutions: contour plot of $\dot{\omega}_{OH}$.

$$\widetilde{Z} = 0.34,\ \widetilde{Z''^2} = 0.024,\ \widetilde{\Lambda} = 0.008,\ \widetilde{\Lambda''^2} = 0.0$$

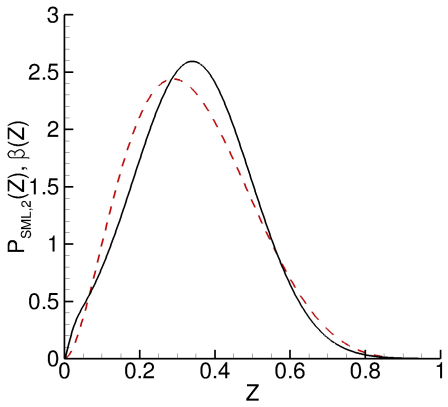

Figure 15: PDFs of Z at the point $(x/d_{ref}, y/d_{ref}) = (8, 0)$ using the values obtained by model B: $P_{SML,2}(Z)$ (black solid line) and $\beta(Z)$ (red dashed line).

$$\widetilde{Z} = 0.065,\ \widetilde{Z''^2} = 0.0012,\ \widetilde{\Lambda} = 0.265,\ \widetilde{\Lambda''^2} = 0.058$$

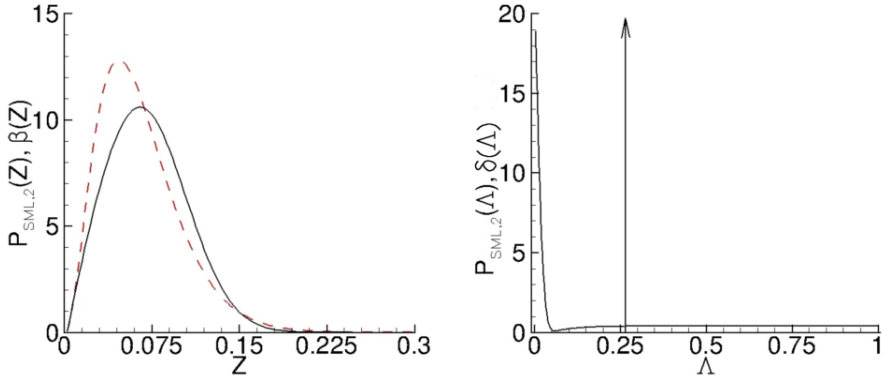

Figure 16: PDFs of Z and Λ at the point $(x/d_{ref}, y/d_{ref}) = (27, 0)$ using the values obtained by model B. Left panel: $P_{SML,2}(Z)$ (black solid line) and $\beta(Z)$ (red dashed line). Right panel: $P_{SML,2}(\Lambda)$ (black solid line) and $\delta(\Lambda)$.

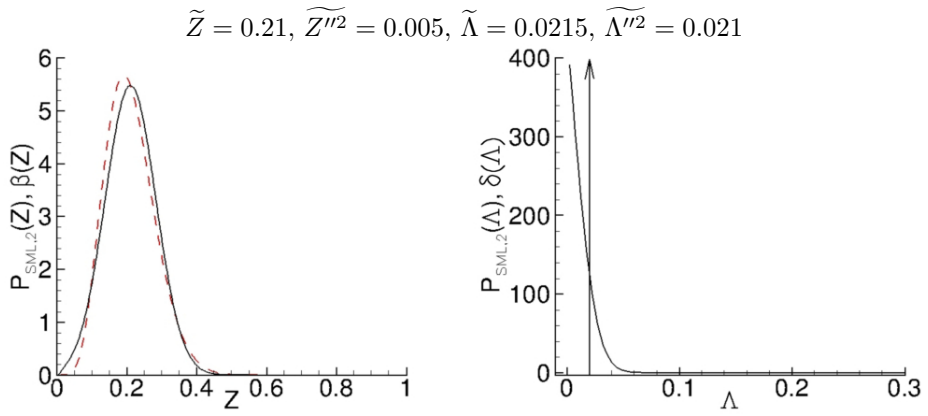

Figure 17: PDFs of Z and Λ at the point $(x/d_{ref}, y/d_{ref}) = (0.85, 0.8)$ using the values obtained by model B. Left panel: $P_{SML,2}(Z)$ (black solid line) and $\beta(Z)$ (red dashed line). Right panel: $P_{SML,2}(\Lambda)$ (black solid line) and $\delta(\Lambda)$.

Table 2: Mean and variance of Z and Λ at three selected points.

		$\widetilde{Z}$	$\widetilde{Z''^2}$	$\widetilde{\Lambda}$	$\widetilde{\Lambda''^2}$
$(x/d_{ref}, y/d_{ref}) = (8, 0)$	Model A	0.37	0.030	0.22	–
	Model B	0.34	0.024	0.008	0
$(x/d_{ref}, y/d_{ref}) = (27, 0)$	Model A	0.085	0.0022	0.56	–
	Model B	0.065	0.0012	0.265	0.058
$(x/d_{ref}, y/d_{ref}) = (0.85, 0.8)$	Model A	0.22	0.007	0.49	–
	Model B	0.21	0.005	0.0215	0.021

mean and variance values of Z and Λ provided in table 2: the mean value of the progress parameter is 0.22 for model A, whereas it is very close to zero for model B. The values of the mixture fraction are very close to each other. Figure 15 shows the corresponding mixture-fraction distributions evaluated by the β-function and by the $P_{SML,2}$ PDF. The two distributions of Λ (not shown) are both Dirac functions since, due to the zero variance, the β-function of model B collapses on a δ-function centred at $\widetilde{\Lambda} = 0.008$.

At the second point on the axis of the burner ($x/d_{ref} = 27$), the reaction is active for both models, as shown by the progress parameter values in table 2, which indicate that the combustion rate is higher for model A. Model B also provides lower values for the mean and variance of the mixture fraction. The PDF of Z and Λ are shown in figure 16. It appears that the $P_{SML,2}$ distribution is close to the β-distribution due to the low variance. The main differences between the two models are clearly observed in the right panel of figure 16, where the $P_{SML,2}(\Lambda)$ and the $\delta(\Lambda)$ are shown in order to put in evidence the inadequate simplification made when assuming the Dirac distribution for the progress parameter.

Finally, considering the third point close to the burner ($x/d_{ref} = 0.85$, $y/d_{ref} = 0.8$), table 2 shows that a large difference in the progress-variable mean value exists between the two models. In fact, model A provides $\widetilde{\Lambda} = 0.49$, indicating that combustion is active, whereas the mean value of Λ for model B is close to zero. Figure 17 shows the corresponding PDF of Z and Λ. Again, the $P_{SML,2}(Z)$ is very close to the β-distribution (left panel), whereas the $P_{SML,2}(\Lambda)$ maintains a smoother behaviour with respect to the δ-function adopted for model A (right panel). The latter difference can be considered a reasonable motivation for the smoother behaviour of the temperature predicted close to the burner by model B (see figures 8 and 9).

5. Conclusions

This paper presents a statistical more likely distribution (SMLD) approach for the evaluation of the presumed probability density function (PDF) in flamelet progress variable (FPV) models for non-premixed supersonic combustion. The FPV model is employed in conjunction with the Reynolds averaged Navier–Stokes (RANS) equations, the temperature field being computed by solving the total energy conservation equation. The proposed SMLD model is built evaluating the most probable joint distribution of the mixture fraction and of the progress variable and its suitability and accuracy are studied in comparison with the standard FPV model. The performance of the standard FPV and of the FPV-SMLD model are discussed by analysing the results of the simulation of a supersonic H_2–Air combustion studied at the NASA Langley Research Center. This analysis shows that the FPV-SMLD model provides an effective improvement over the standard approach and is able to properly describe the flame structure in good agreement with the results obtained by highly resolved LES with detailed chemistry. In fact, the numerical results correctly predict the presence of the three characteristic regions of supersonic flames: the autoignition, the stabilization and the combustion regions. Moreover, the FPV-SMLD model can correctly evaluate the lift-off of the flame whereas the standard model is not able to predict the combustion kinetic with sufficient accuracy, providing a sudden ignition of the mixture close to the burner inlet. A detailed analysis of the PDF distributions at three points of the computational domain is provided in order to quantify and explain the differences between the two models. This work has shown that indeed evaluating the PDF using the SMLD approach allows one to improve the accuracy of the simulation of a reacting supersonic flow when solving the RANS equations. However, several aspects should be considered to enhance this analysis, such as: the effects of compressibility deserve to be analyzed in more details employing, for instance, a compressible FPV model; the effects of the hypothesis that the mixture fraction and the progress variable are not statistically independent should be studied; the influence of the proposed FPV-SMLD model in the LES framework should be investigated. All this issues go beyond the aim of the present paper and will be the subject of future work.

Acknowledgements

This research has been supported by grant n. $PON03PE\_00067\_6$ APULIA SPACE. The authors are very grateful to M. D. de Tullio for his support in the software development and to T.S. Cheng for providing the experimental data used as reference. Then, the authors wish to thanks P. Boivin for providing numerical LES results used as reference and for the interesting and useful discussion.

References

[1] D. Cecere, E. Giacomazzi, A. Ingenito, A review on hydrogen industrial aerospace applications, International Journal of Hydrogen Energy 39 (2014) 10731–10747.

[2] T. S. Cheng, J. A. Wehrmeyer, R. W. Pitz, Simultaneous temperature and multispecies measurement in a lifted hydrogen diffusion flame, Combust. Flame 91 (3) (1992) 323–345.

[3] M. Stöllinger, S. Heinz, Evaluation of scalar mixing and time scale models in PDF simulations of a turbulent premixed flame, Combustion and Flame 157 (9) (2010) 1671–1685.

[4] S. Lu, J. Fan, K. Luo, High-fidelity resolution of the characteristic structures of a supersonic hydrogen jet flame with heated co-flow air, International Journal of Hydrogen Energy 37 (2012) 3528–3539.

[5] T. Jin, K. Luo, S. Lu, J. Fan, DNS investigation on flame structure and scalar dissipation of a supersonic lifted hydrogen jet flame in heated coflow, International Journal of Hydrogen Energy 38 (23) (2013) 9886–9896.

[6] D. Cecere, A. Ingenito, E. Giacomazzi, L. Romagnosi, C. Bruno, Hydrogen/air supersonic combustion for future hypersonic vehicles, International Journal of Hydrogen Energy 36 (2011) 11969–11984.

[7] P. Boivin, A. Dauptain, C. Jimnez, B. Cuenot, Simulation of a supersonic hydrogen-air autoignition-stabilized flame using reduced chemistry, Combustion and Flame 159 (4) (2012) 1779–1790.

[8] F. Williams, Detailed and reduced chemistry for hydrogen autoignition, Journal of Loss Prevention in the Process Industries 21 (2) (2008) 131–135.

[9] L. V. Bezgin, V. I. Kopchenov, A. S. Sharipov, N. S. Titova, A. M. Starik, Evaluation of prediction ability of detailed reaction mechanisms in the combustion performance in hydrogen/air supersonic flow, Combust. Sci. Technol 185 (2013) 62–94.

[10] U. Maas, S. Pope, Simplifying chemical kinetics- intrinsic low-dimensional manifolds in composition space, Combust. Flame 88 (1992) 239–264.

[11] C. Pierce, Progress-variable approach for large-eddy simulation of turbulent combustion, PhD Thesis, Stanford University (2001).
[12] O. Gicquel, N. Darabiha, D. Thevenin, Laminar premixed hydrogen/air counterflow flame simulations using flame prolongation of ILDM with differential diffusion, Proc. Combust. Inst. 28 (2000) 1901–1908.
[13] J. V. Oijen, L. D. Goey, Modelling of premixed laminar flames using flamelet-generated manifolds, Combust. Sci. Technol. 161 (2000) 113–137.
[14] N. Peters, Turbulent combustion, Cambridge University Press, 2000.
[15] C. D. Pierce, P. Moin, Progress-variable approach for large-eddy simulation of non-premixed turbulent combustion, J. Fluid Mech. 504 (2004) 73–97.
[16] H. Pitsch, N. Peters, A consistent flamelet formulation for non-premixed combustion considering differential diffusion effects, Combustion and Flame 114 (12) (1998) 26 – 40.
[17] D. Carbonell, C. Perez-Segarra, P. Coelho, A. Oliva, Flamelet mathematical models for non-premixed laminar combustion, Combustion and Flame 156 (2) (2009) 334 – 347.
[18] E. Knudsen, H. Pitsch, A general flamelet transformation useful for distinguishing between premixed and non-premixed modes of combustion, Combustion and Flame 156 (3) (2009) 678 – 696.
[19] E. Knudsen, H. Pitsch, Capabilities and limitations of multi-regime flamelet combustion models, Combustion and Flame 159 (1) (2012) 242 – 264.
[20] M. Oevermann, Numerical investigation of turbulent hydrogen supersonic combustion is a scramjet using flame let modeling, Aerosp. Sci. Technol. 4 (2000) 463–480.
[21] L. Hou, D. Niu, Z. Ren, Partially premixed flamelet modeling in a hydrogen-fueled supersonic combustor, International Journal of Hydrogen Energy 39 (17) (2014) 9497 – 9504.
[22] R. Pecnik, V. E. Terrapon, F. Ham, G. Iaccarino, H. Pitsch, Reynolds-Averaged NavierStokes Simulations of the HyShot II Scramjet, AIAA Journal 50 (8) (2012) 1717–1732.
[23] A. Saghafian, V. E. Terrapon, H. Pitsch, An efficient flamelet-based combustion model for compressible flows, Combustion and Flame 162 (3) (2015) 652 – 667.
[24] S. Pope, PDF methods for turbulent reactive flows, Prog. Energy Combust. Sci. 11 (1985) 119–192.
[25] M. Ihme, H. Pitsch, Prediction of extinction and re-ignition in non-premixed turbulent flames using a flamelet progress variable model. 1 A priori study and presumed PDF, Combust. Flame 155 (2008) 70–89.
[26] M. Ihme, L. Shunn, J. Zhang, Regularization of reaction progress variable for application to flamelet-based combustion models, J. Comput. Phys. 231 (2012) 7715–7721.
[27] A. Najafi-Yazdi, B. Cuenot, L. Mongeau, Systematic definition of progress variables and intrinsically low-dimensional, flamelet generated manifolds for chemistry tabulation, Combust. Flame 159 (2012) 1197–1204.
[28] Y.-S. Niu, L. Vervisch, P. D. Tao, An optimization-based approach to detailed chemistry tabulation: Automated progress variable definition, Combust. Flame 160 (2013) 776785.
[29] H. Pitsch, M. Chen, N. Peters, Unsteady flamelet modelling of turbulent hydrogen/air diffusion flames, Proceeding of the Combustion Institute 27 (1998) 1057–1064.
[30] J. S. Kim, F. A. Williams, Structures of flow and mixture-fraction fields for counterflow diffusion flames with small stoichiometric mixture fractions, Journal of Applied Mathematics 53 (1993) 1551–1566.
[31] N. Peters, Laminar diffusion flamelet models in non-premixed turbulent combustion, Prog. Energy Combust. Sci. 10 (1984) 319–339.
[32] M. Ihme, C. M. Cha, H. Pitsch, Prediction of local extinction and re-ignition effects in non-premixed turbulent combustion using a flamelet/progress variable approach., Proc. Combust. Inst. 30 (2005) 793–800.
[33] M. Ihme, H. Pitsch, Prediction of extinction and re-ignition in non-premixed turbulent flames using a flamelet progress variable model. 2 Application in LES of Sandia Flames D and E, Combust. Flame 155 (2008) 90–107.
[34] R. De Meester, B. Naud, B. Merci, A priori investigation of pdf-modeling assumptions for a turbulent swirling bluff body flame ('sm1'), Combustion and Flame 159 (11) (2012) 3353–3357.
[35] S. Mukhopadhyay, J. Abraham, Evaluation of an unsteady flamelet progress variable model for autoignition and flame development in compositionally stratified mixtures, Phys. Fluids 24 (2012) 075115.
[36] A. Coclite, G. Pascazio, P. De Palma, L. Cutrone, M. Ihme, An SMLD joint PDF model for turbulent non-premixed combustion using the flamelet progress-variable approach, Flow, Turbulence and Combustion 95 (1) (2014) 97–119.
[37] L. Cutrone, P. De Palma, G. Pascazio, M. Napolitano, A RANS flamelet-progress-variable method for computing reacting flows of real-gas mixtures, Comput. Fluids 39 (2010) 485–498.
[38] A. W. Cook, J. J. Riley, A subgrid model for equilibrium chemistry in turbulent flows, Phys. Fluids 6 (1994) 2868–2870.
[39] J. Jimenez, A. Linan, M. M. Rogers, F. J. Higuera, A priori testing of subgrid models for chemically reacting non-premixed turbulent shear flows, J. Fluid Mech. 349 (1997) 149–171.
[40] C. Wall, B. J. Boersma, P. Moin, An evaluation of the assumed beta probability density function subgrid-scale model for large eddy simulation of non-premixed, turbulent combustion with heat release, Phys. Fluids 12 (2000) 2522–2529.
[41] D. A. Schwer, Numerical study of unsteadiness in non-reacting and reacting mixing layers, PhD Thesis, The Pennsylvania State University (1999).
[42] P. Saxena, F. Williams, Testing a small detailed chemical-kinetic mechanism for the combustion of hydrogen and carbon monoxide, Combustion and Flame 145 (1-2) (2006) 316–323.
[43] H. Pitsch, Flamemaster v3.3. A C++ computer program for 0d combustion and 1d laminar flame calculations.
[44] J. L. Steger, R. F. Warming, Flux vector splitting of the inviscid gas-dynamic equations with applications to finite difference methods, J. Comput. Phys. 40 (1981) 263–293.
[45] T. H. Pulliam, D. S. Chaussee, A diagonal form of an implicit factorization algorithm, J. Comput. Phys. 39 (1981) 347–363.

[46] P. E. O. Buelow, D. A. Schwer, J.-Z. Feng, C. L. Merkle, D. Choi, A preconditioned dual time diagonalized ADI scheme for unsteady computations, in: AIAA Proceedings, 1997.
[47] F. Menter, C. Rumsey, Assessment of two-equation turbulence models for transonic flows, in: 25^{th} AIAA Fluid Dynamics Conference, AIAA, Colorado Springs, CO, 1994.
[48] T. Cheng, J. Wehrmeyer, R. Pitz, O. Jarrett Jr., G. Northam, Raman measurement of mixing and finite-rate chemistry in a supersonic hydrogen-air diffusion flame, Combustion and Flame 99 (1) (1994) 157–173.
[49] T. Bridel-Bertomeu, P. Boivin, Explicit chemical timescale as a substitute for tabulated chemistry in a h2o2 turbulent flame simulation, Combustion Science and Technology (2014) null.
[50] Y. Moule, V. Sabelnikov, A. Mura, Highly resolved numerical simulation of combustion in supersonic hydrogenair coflowing jets, Combustion and Flame (0) (2014) –.